Phase sensitive optical coherence microscopy for photothermal imaging of gold nanorods

Yong Hu, Adrian Gh. Podoleanu, George Dobre

Yong Hu, Adrian Gh. Podoleanu, George Dobre, "Phase sensitive optical coherence microscopy for photothermal imaging of gold nanorods," Proc. SPIE 10591, 2nd Canterbury Conference on OCT with Emphasis on Broadband Optical Sources, 105910E (5 March 2018); doi: 10.1117/12.2285816

SPIE.

Event: Second Canterbury Conference on Optical Coherence Tomography, 2017, Canterbury, United Kingdom

Phase sensitive optical coherence microscopy for photothermal imaging of gold nanorods

Yong Hu*, Adrian Gh. Podoleanu, George Dobre
Applied Optics Group, University of Kent, Canterbury, United Kingdom, CT2 7NH,
*yh95@kent.ac.uk

ABSTRACT

We describe a swept source based phase sensitive optical coherence microscopy (OCM) system for photothermal imaging of gold nanorods (GNR). The phase sensitive OCM system employed in the study has a displacement sensitivity of 0.17 nm to vibrations at single frequencies below 250 Hz. We demonstrate the generation of phase maps and confocal phase images. By displaying the difference between successive confocal phase images, we perform the confocal photothermal imaging of accumulated GNRs behind a glass coverslip and behind the scattering media separately. Compared with two-photon luminescence (TPL) detection techniques reported in literature, the technique in this study has the advantage of a simplified experimental setup and provides a more efficient method for imaging the aggregation of GNR. However, the repeatability performance of this technique suffers due to jitter noise from the swept laser source.

Keywords: phase sensitive, optical coherence microscopy, photothermal imaging

1. INTRODUCTION

Due to its high sensitivity, the technology of phase sensitive interferometry has been applied to characterize the curvature and the precession angle of a liquid mirror [1, 2]. In the technique, both the curvature and precession angle of the liquid mirror are measured by generating phase maps. The interferometric phase was retrieved from the coherent interference between a reference Bessel beam and another coherent beam reflected by the liquid mirror. The phase map appearing as concentric annulus is intrinsically the interference pattern. However, as the laser beam employed in the technique is in the CW mode, even though the phase measurement provides high sensitivity, this technology is not able to perform a depth resolved detection. Optical Coherence Microscopy (OCT) is also capable of high sensitivity, and has the added advantage of being able to perform depth resolved detection. OCM combines the coherent detection methods of OCT with the confocal microscopy, which enhances penetration depth compared to standard confocal microscopy and dramatically improves the resolution over cross-sectional OCT imaging [3].

Gold nanoparticles (GNPs) are outstanding contrast and therapy agents in biomedical imaging and photothermal therapeutics [4]. They possess useful optical properties that can be tuned to absorb and scatter light across the visible and near-IR region. These properties are heavily determined by precise control over the particles' shape, size, architecture or environment [5]. As the earliest developed GNPs, gold nano-spheres are not optimized in biomedical applications due to their limited peak absorptions in the transmission window (650-900 nm) for biological entities [6]. By contrast, gold nano-shells (GNSHs) and gold nano-rods (GNRs) have tunable peak absorption wavelengths in a wider electromagnetic range [7,8]. Compared with GNSHs (hundreds of nanometers in size), GNRs have the advantage in vivo molecular imaging due to their smaller size scale (tens of nanometers). Moreover, as GNRs process higher photothermal conversion efficiencies in the NIR region than GNSHs, GNRs are more interested agents in photothermal therapeutics compared to GNSHs [9].

Two-photon luminescence (TPL) detection has been reported for imaging the aggregated GNRs exposed to a Ti:Sa laser beam [10]. However, as the generated TPL signal was weak, the TPL detection was only achieved to GNRs diffused in clear media, not in biological tissue or other scattering media. As 96% of the absorbed energy of GNRs to the Ti:Sa beam is converted into heat [10], we anticipate that measuring the temperature variation induced by the photothermal effect should be a more efficient method than TPL to detect the existence of GNRs. In this study, we employ a swept source based phase sensitive OCM system to image GNRs behind scattering media by imaging their photothermal effect.

2nd Canterbury Conference on OCT with Emphasis on Broadband Optical Sources,
edited by Adrian Podoleanu, Ole Bang, Proc. of SPIE Vol. 10591, 105910E
 · doi: 10.1117/12.2285816

2. EXPERIMENT SETUP

Fig. 1 shows the configuration of the phase sensitive OCM system implanted with photothermal modulation devices. A Ti:Sa beam (Coherent, @ 800 nm, 30 nm bandwidth) is coaxially combined with the swept source beam (Axsun, @ 1060 nm, 100 nm bandwidth). A optics shutter is used to enable or disable the Ti:Sa beam to the OCM system. The swept source beam enters a fiber based Michelson interferometer with three collimators launching 2.4 mm wide beam. 80% of the light proceeds to the reference arm, and the remaining 20% to the sample arm. In the sample arm, the combined beams hit a pair of galvanometer mirrors (THORLABS, GVS302) and subsequently an objective/scan lens (THORLABS, LSM02-BB, f =18 mm) that produces a focused spot size of 3.1 µm. In the reference arm, the beam propagates through two glass made dispersion compensation blocks (THORLABS, LSM02DC), so that the dispersion in this arm matches the dispersion created by the double-path of the objective in the sample arm. Light beams returning from both arms interfere at the output of the interferometer. The interference signal is detected by a balanced photodetector (THORLABS, PDB430C DC to 350 MHz bandwidth) that removes the DC component in the signal. The signal is then acquired by a 12 bit waveform digitizer (AlazarTech, ATS9350, sampling rate 500 MS/s) installed in the computer. The digitizer has two trigger receiving ports, one of which is connected to the output trigger on the swept laser. As the swept laser starts each spectral sweep with exporting a trigger output, this connection enables the synchronization between the spectral sweep and the A-scan data acquisition. The other input port on the digitizer is connected to the *k*-clock output on the swept laser. As the spectral sweep of the laser generates a clock nonlinear in the time domain but uniform in the *k*-space, this connection enables the digitizer to perform uniformly data sampling in the *k*-space while generating the interference spectrum. Thus, no extra data resampling or processing is required. Then, the digitized interference spectrum of each A-scan is complex Fourier transformed to extract the depth-resolved intensity profile $A(z)$ and phase profile $\Phi(z)$ of the sample. The front surface of the coverslips in Fig. 1.A and Fig. 1.B provide the reference phase $\Phi(z_0)$. By subtracting $\Phi(z_0)$ from $\Phi(z)$, it is applicable to remove the common mode noise created from mechanical or thermal fluctuations in each independent arm.

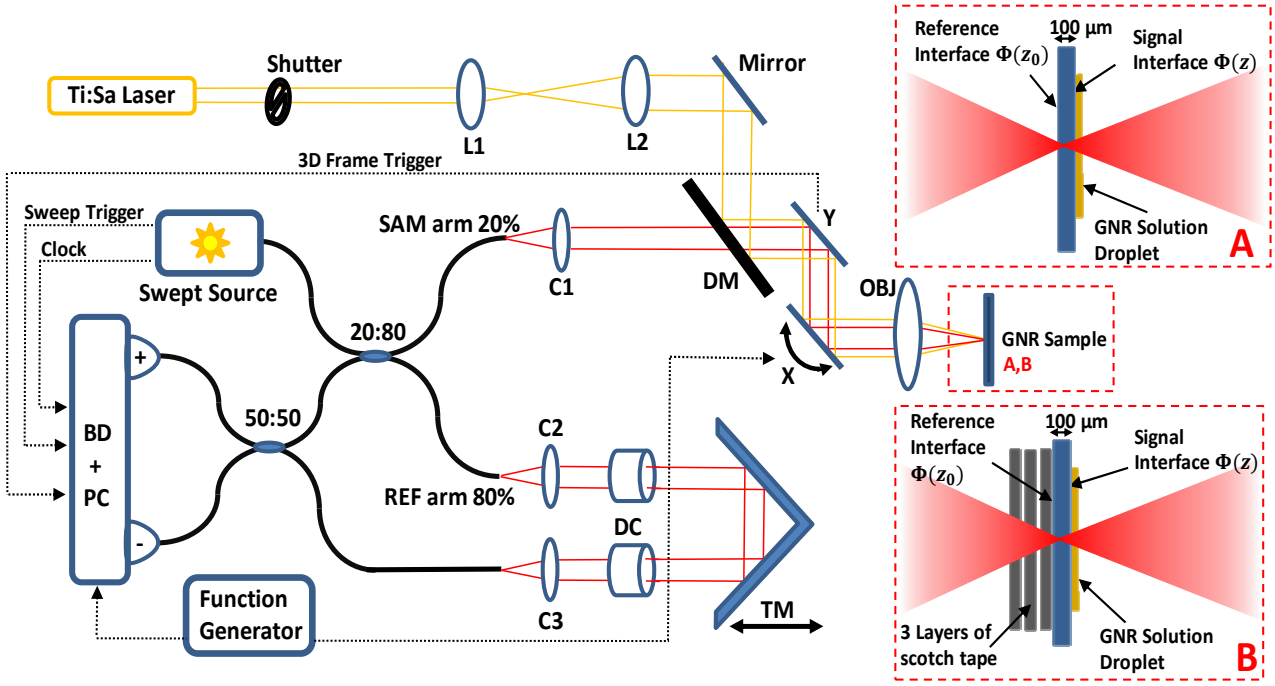

Fig. 1. Schematic layout of the phase sensitive OCM with photothermal modulation system. Superluminescent diode (SLD), collimating lenses (C1, C2, C3), doublets lengths (L1, L2), dichroic mirror (DM), scanning mirrors (X, Y), objective lens (OBJ), dispersion compensating block (DC), transmission mirrors (TM), balanced photodetector (BD), computer (PC). The sample is replaced by inserts (A): a GNR solution droplet on the back surface of a coverslip; (B): 3 layers of scotch tape are stuck on the front surface of the coverslip to simulate scatters.

The phase information was retrieved by the following procedures: (1) for each A-scan, 1024 samples were recorded to construct the interference spectrum. (2) This spectrum was then complex Fourier transformed to produce a 512-pixel A-scan intensity profile. (3) the pixel location of the A-scan peak corresponding to the reflection event from the reference interface (i.e. the air-glass interface in Fig. 1.A and Fig. 1.B) was identified to provide $\Phi(z_0)$. (4) the pixel order number

corresponding to the interested location was selected to provide $\Phi(z)$. (5) in the A-scan phase profile, the phase value $\Phi(z)$ of the selected pixel order number was retrieved. In practice, the difference between $\Phi(z)$ and $\Phi(z_0)$ was used as the signal to build the phase map.

3. SYNCHRONIZATION

For the OCM system, it is critical to synchronize the swept laser and galvo scanners with the data acquisition and the image processing. Based on the configuration in Fig. 1, the swept laser sends out a trigger signal at the beginning of each sweep. On receiving the trigger signal, the digitizer starts to record 1024 data to generate an A-scan interference spectrum as the sweep going. As the sweep rate is 100 kHz, the determined A-scan acquisition rate is 100 kHz, i.e. 10 μs for each A-scan. The 10 μs is the total time for the sweep cycle of the swept laser, including a 5 μs forward sweep and a 5 μs backward sweep. In the practice, the interference fringe generated from the forward sweep was recorded, leaving out the one generated from the backward sweep. Thus, the digitizer is required to acquire data only in the first 5 μs, leaving the remaining 5 μs waiting for the next sweep trigger signal from the laser. To this end, the sampling rate of the digitizer was set to be 250 MS/s so that it took 4.1 μs for sampling 1024 data, which captured 4/5 of the 5 μs. Consequently, the spectral sweep of the laser and the data acquisition of the digitizer starts at the same time, and they step into the data acquisition progress together to fully use the sweeping spectrum of the laser. In the remaining 5 μs, the LabVIEW programme performs the complex Fourier transform to the digitized interference spectrum, generates the A-scan profile, and then displays it on the monitor. During this 5 μs, the digitizer is waiting for the trigger for the next spectral sweep. Thus, in the A-scan operating mode, the OCM system operates at 100 kHz, with 5 μs acquiring data and 5 μs processing data.

To generate phase maps, both galvo scanners were enabled. One scanner was activated to raster the beam at 250 Hz, equivalent to 2 ms forward scanning and 2 ms backward scanning in each cycle. In each 2 ms, 200 A-scan spectral spectra were recorded to generate a B-scan image. The other scanner was activated by a sawtooth wave function at 1.25 Hz, with 800 ms ramping upward and then sharply dropping back. To synchronize the moving of these two galvo scanners with a 3D data acquisition, a trigger signal was sent out from the slower scanner to the digitizer when the slower scanner was ready to ramp upward. In the following 800 ms, the faster galvo produced 200 cycles, and the digitizer recorded 400 A-scan interference spectra in each cycle, with 200 A-scans in the forward scanning and 200 A-scans in the backward scanning. During this 800 ms, the digitizer buffered all 80000 A-scan interference spectra into the memory. 800 ms latter, a LabVIEW programme cut these 80000 A-scan data into a 200×400 array. As every element in the array was an A-scan interference spectrum consisting 1024 data, the structured 3D data had a volume of 200×400×1024 pixels. Because the faster scanner scanned the same line twice, forward and backward, the 3D data had a mirror term. We left out the mirror term and made a 200×200×1024 array that was then mapped to the grayscale to produce a 3D image of the detected sample. Thus, in the 3D operating mode, the system operated at 1.25 Hz and generated 3D images composed of 200×200×1024 pixels.

4. RESULTS

4.1 Phase map and *en-face* phase image generation

We performed the 3D detection on the sample in Fig. 1.A. Results are presented in Fig. 2. As the OCM system is depth resolved, $A(z)$ is retrieved to generate the confocal microscopy image (Fig. 2.A) of the front surface and the microscopy image (Fig. 2.B) of the back surface of the coverslip, whereas $\Phi(z)$ is retrieved to generate phase maps (Fig. 2.a and Fig. 2.b) of these two surfaces. Dusts on the front surface of the coverslip are shown in both the microscopy image (Fig. 2.A) and the phase map (Fig. 2.B). The GNR solution droplet on the back surface of the coverslip is displayed in the microscopy image (Fig. 2.B) and the phase map (Fig. 2.b). Subtracting Fig. 2.a from Fig. 2.b, the *en-face* phase image (Fig. 2.c) displays the features of the GNR solution droplet in the phase manner.

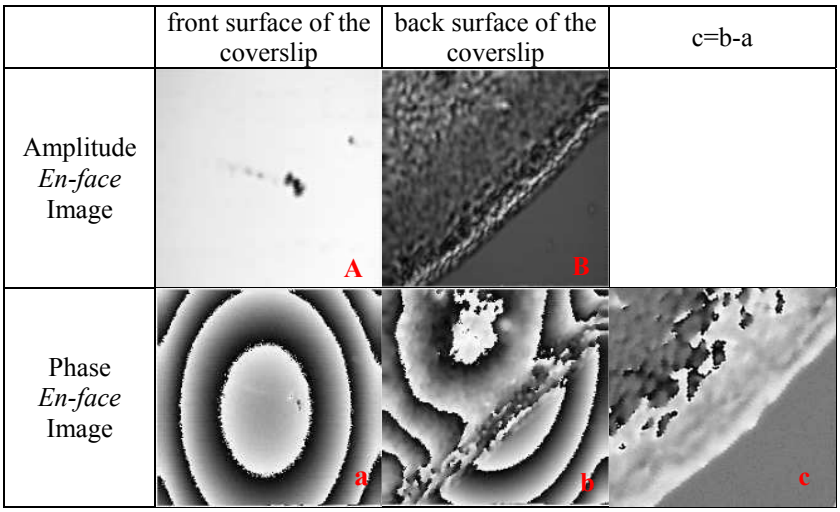

Fig. 2. (A) and (B): microscopy images of the front surface and the back surface of the coverslip in Fig. 1.A; (a) and (b): phase maps of the front surface and the back surface of the coverslip in Fig. 1.A; (c): *en-face* phase image obtained by subtracting (a) from (b). Image size: 60×60 μm.

As seen in Fig. 2, compared with the microscpy image (Fig. 2.B), the en-face phase image (Fig. 2.c) loses most of the details of the droplet. The fine structure of the droplet surface, particularly the granularity, can be seen in the microscopy image (Fig. 2.B) but not in the phase image (Fig. 2.c). This is because the phase value retrieved from the OCM system is wrapped between 0 and 2π, and any measured phase value larger than 2π is set to a grayscale corresponding to exactly 2π.

4.2 Photothermal modulation and *en-face* phase imaging

The sample used here is the one used in section 4.1. While the system was running and displaying *en-face* phase images of the back surface of the coverslip with the GNR solution droplet, we enabled and disabled the exposure of the Ti:Sa beam on the sample by controlling the shutter in Fig. 1.

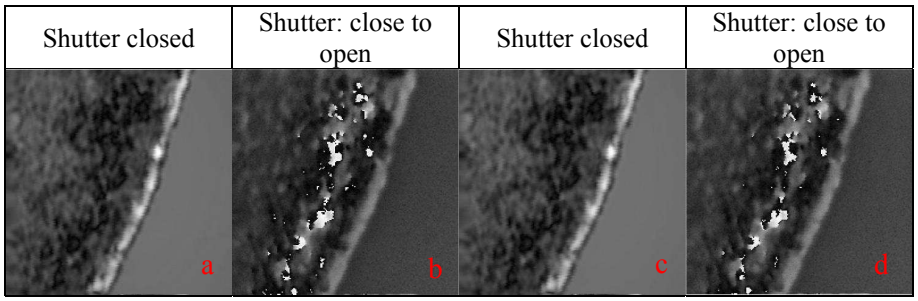

Fig. 3. (a) and (c): *en-face* phase images when the shutter is closed; (b) and (d): *en-face* phase images when the shutter is switched from closed to open. Image size: 60×60 μm.

Results are shown in Fig. 3. As seen, when the shutter is switched from closed to open, a clear photothermal effect is detected, showing GNRs excited by the Ti:Sa beam. The en-face phase images show different features when the GNR sample is modulated by the Ti:Sa beam, proving that phase sensitive OCM system can be used for photothermal imaging of GNRs.

4.3 Photothermal imaging of GNRs

Although we have proved that the phase sensitive OCM can be used for imaging the photothermal effect of GNRs, the contrast of the images in section 4.2 is not optimized.

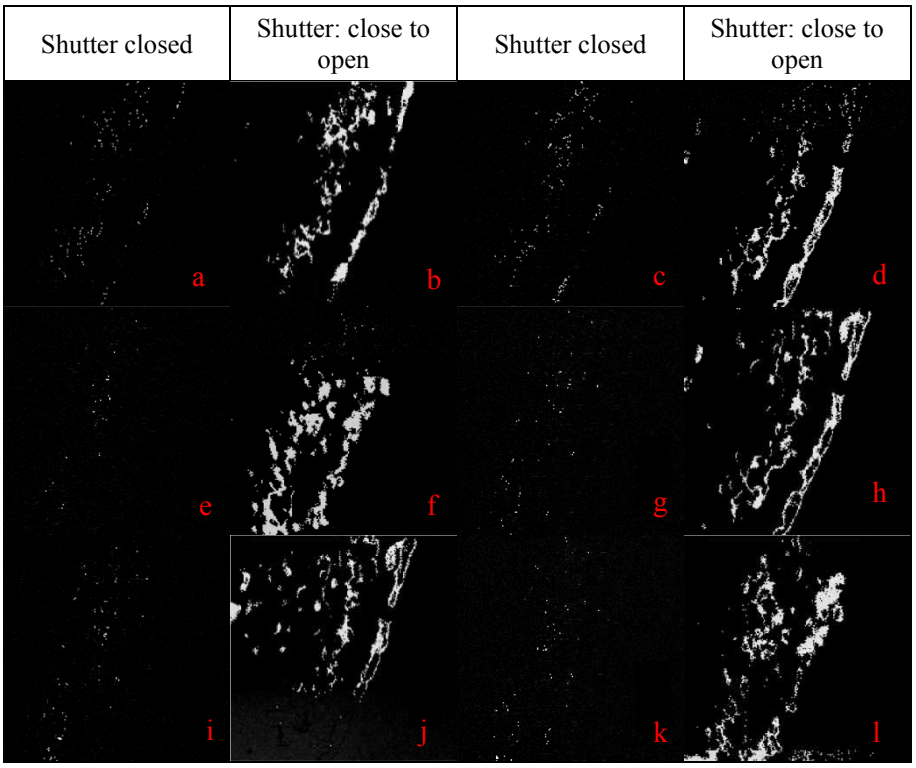

Fig. 4. Images displaying the difference between successive *en-face* phase images. The GNR solution droplet is on the back surface of the coverslip in Fig. 1.A. Image size: 60×60 μm.

In order to improve the image contrast and highlight the features induced by the photothermal modulation of the Ti:Sa beam, instead of displaying the dynamic *en-face* phase image, we display the difference between successive *en-face* phase images. As seen in Fig. 4.(a), (c), (e), (g), (i) and (k), when the Ti:Sa beam to the sample is blocked, the difference between successive *en-face* phase images is zero, representing as dark images. These images are not completely dark due to the scanning error of the galvo-scanners. As seen in Fig. 4.(b), (d), (f), (h), (j) and (l), when the shutter is open to enable the Ti:Sa beam to the GNRs sample, images with optimized contrast are obtained. The locations of GNRs are shown as bright features in these images. Thus, by displaying the difference between successive *en-face* phase images, the GNRs are allocated more accurately than displaying the *en-face* phase images. However, each time the shutter moves from closed to open, the patterns in Fig. 4.(b), (d), (f), (h), (j) and (l) vary. The poor reproducibility of the technique is the net result of the jitter noise existing in the swept source. The jitter noise comes from fluctuations in the relative phase between successive spectral sweeps in the laser source.

4.4 Photothermal imaging of GNRs behind scattering media

The same technique was applied to image the GNRs in scattering media. As shown in Fig. 1.B, three layers of adhesive tape were applied to the front surface of the coverslip to simulate a scattering medium, and the experiment process described in section 4.3 was carried out. As seen in Fig. 1.B, the beam goes through the scattering layers of tape, hits the tape/glass interface providing the reference phase $\Phi(z_0)$ and then hits the glass/GNR interface providing the signal phase $\Phi(z)$. The result images displaying the difference between successive *en-face* phase images are presented in Fig. 5. They indicate that the technique is capable of photothermal imaging of GNRs behind scatters. Every time the shutter switches from closed to open, the location of GNRs behind scatters is imaged by the phase sensitive OCM system. Once again, due to the jitter noise from the swept source, the patterns in Fig. 5.(b), (d), (f), (h), (j) and (l) are different.

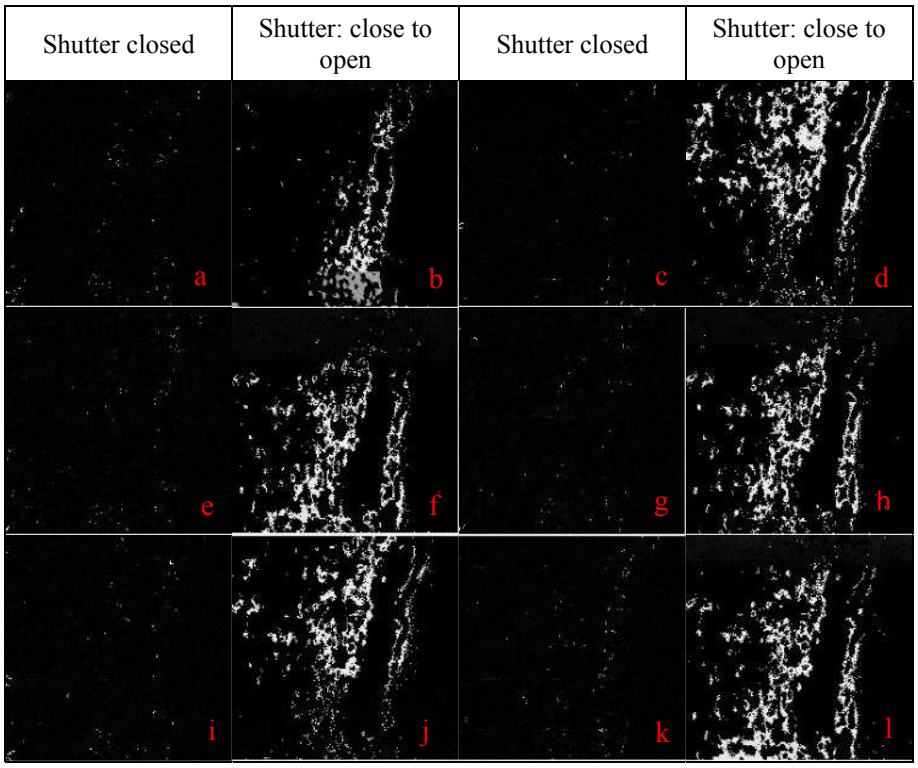

Fig. 5. Images displaying the difference between successive *en-face* phase images. GNRs are on the back surface of the coverslip in Fig. 1.B. Image size: 60×60 μm.

5. CONCLUSIONS

We prove that the phase sensitive OCM system is capable of photothermal imaging of accumulated GNRs behind the scattering medium. It is an alternative and advanced technique to the TPL technique which was previously reported to detect and image GNRs in clear medium. In order to minimize the measurement error given by the surroundings, in addition to measure the signal phase at the interested depth, we measured a reference phase on a clean and stationary reference interface. By subtracting the reference phase from the signal phase, the phase variation created by the moving air and the vibration of components in the setup is eliminated. In order to maximize image contrast, instead of displaying the *en-face* phase image, we designed and built a software utility that displays the difference between successive *en-face* phase images showing in grayscale. Although this technique offers improved image contrast, its measurement repeatability is degraded by the jitter noise from the swept laser source. To solve the problem, an external trigger fixing the relative phase value between successive spectral sweeps should be implemented between the laser source and the interferometer in the future study. Besides, to solve the 2π ambiguity in the *en-face* phase image, a suitable phase unwrap algorithm is desirable.

REFERENCES

[1] M. Fortin, M. Piche, and E. F. Borr, "Optical tests with Bessel beam interferometry," Opt. Exp. 12(24), 5887-5895 (2004).
[2] B. Bélanger, X. Zhu, et M. Piché, "Auto-imagerie à l'aide de faisceaux non-diffractants," Phys. Can. 52, 160-161 (1996).
[3] J. A. Izatt, M. R. Hee, G. M. Owen, E. A. Swanson, and J. G. Fujimoto, "Optical coherence microscopy in scattering media," Opt. Lett. **9**(8), 590-592 (1994).
[4] I. A. Wani, "Biomedical Applications of Gold Nanoparticles: Recent Advances and Future Prospects," in Biomedical Engineering: Concepts, Methodologies, Tools, and Applications, IRMA, (IGI Global, 2017).
[5] J. Stone, St. Jackson, and D. Wright, "Biological applications of gold nanorods," NanoMed. and NanoBio. **3**(1), 100 (2010).

[6] Ch. Schoen, "Gold Nanostructures: Properties and Applications," http://www.sigmaaldrich.com/technical-documents/articles/materials-science/nanomaterials/gold-nanostructures.html
[7] H. Chen, E. Gratton, and M. A. Digman, "Self-assisted optothermal trapping of gold nanorods under two-photon excitation," Methods Appl. Fluoresc. **4**(3), 035003 (2016).
[8] S. J. Oldenburg, J. B. Jackson, S. L. Westcott, and N. J. Halas, "Infrared extinction properties of gold nanoshells," Appl. Phys. Lett. **75**(19), 2897-2899 (1999).
[9] T. Niidome, M. Yamagata, Y. Okamoto, Y. Akiyama, H. Takahashi, T. Kawano, Y. Katayama, and Y. Niidome, "PEG-modified gold nanorods with a stealth character for in vivo applications," J Control Release **114**(3), 343-347(2006).
[10] H. Chen, E. Gratton, and M. A. Digman, "Self-assisted optothermal trapping of gold nanorods under two-photon excitation," Methods Appl. Fluoresc. **4**(3), 035003 (2016).